5-2015

Steps Toward Precision Measurements on Molecular Ions

Edward Bell
Clemson University

Follow this and additional works at: https://tigerprints.clemson.edu/all_theses

STEPS TOWARD PRECISION MEASUREMENTS ON MOLECULAR IONS

A Thesis
Presented to
the Graduate School of
Clemson University

In Partial Fulfillment
of the Requirements for the Degree
Master of Science
Physics

---

by
Edward Bell
May 2015

Accepted by:
Dr. Joan Marler, Committee Chair
Dr. Chad Sosolik
Dr. Marcin Ziolkowski

Abstract

This thesis is a review of the work performed to assist future studies in the Ion Trapping Lab. This includes the results of calculations using *ab initio* quantum chemistry techniques on the CaH^+ molecular ion. Ground state potential energy surfaces of the CaH^+ molecular ion for geometries 0.5Å$\leq$ R $\leq$ 10.45Å in steps of 0.05Å were calculated using correlation consistent basis sets at the CCSD and CCSD(T) level of theory. The dependence of SCF, CCSD correlation, and CCSD(T) correlation energies on basis set size was analyzed in detail near the well and near the asymptote. The extrapolated correlation energy for an infinite basis set was calculated for each geometry at the CCSD(T) level of theory. Effects due to correlation of core electrons were explored at the CCSD and CCSD(T) level of theory. Ground state potential energy surfaces with polarization functions added to the core orbitals of the calcium atom were also calculated at the CCSD and CCSD(T) level of theory. Additionally, a UHV compatible oven to vaporize neutral calcium and a PZT driver circuit were designed and constructed. This instrumentation will facilitate precision measurements on ions and molecular ions.

Contents

List of Tables

List of Figures

Chapter 1

Introduction

Ion traps provide an ideal experimental set up to investigate properties of atomic and molecular ions. Electromagnetic fields can be used to confine these systems. The two types of traps that are most commonly used are Paul and Penning traps. Penning traps rely on a magnetic field to confine ions radially as well as an electric field to confine them axially. Paul traps use an oscillating electric field to confine the ions radially. A static electric field is used to confine the ions axially.
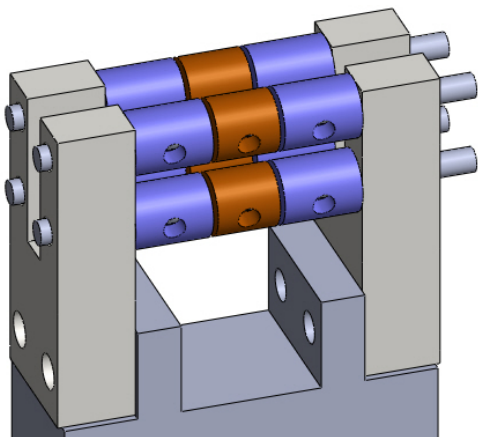
Figure 1.1: A rendering of the linear Paul trap design that will be used to trap atomic and molecular ions. A constant voltage is applied to each of the end caps(blue) to confine the ions axially. An oscillating voltage is applied to each of the center electrodes (orange) to confine the ions radially.
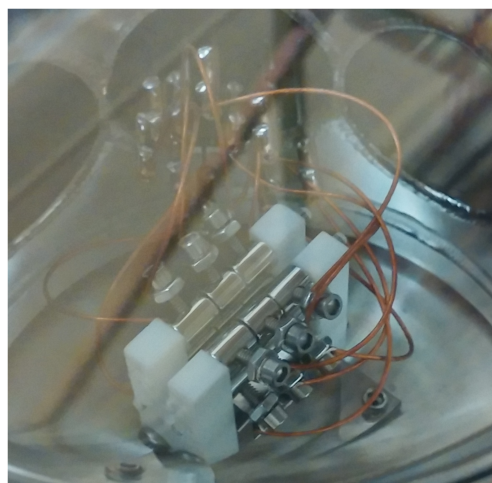
Figure 1.2: The Paul trap is mounted on a pedestal and is centered within the vacuum chamber. Ionizing, cooling, and probe laser beams pass through the center of the trap. Copper wires carry the appropriate signal to each electrode.

Precision laser spectroscopy can be used to study properties of trapped atomic and molecular ions. These include, but are not limited to, reactions at millikelvin temperatures, probing intermediate dynamics in reactions, measuring reaction rates of different species, and charge exchange between different species. Ion traps can also be used to trap molecular ions. Laser cooling of molecular ions is possible, but sympathetic cooling of co-trapped species is more practical. Rovibrational states of molecular ions are probed using a variety of spectroscopic techniques.

Trapped atomic and molecular ions are used to experimentally test predictions made by modern theories. Possible variation of the fine structure constant is measured using transition frequencies of trapped ionic species. The ratio of measured transition frequencies of Ag^+ and Hg^+ ions was used to calculate deviation in α. [1] This experiment found a deviation of $(d\alpha/dt)/\alpha = $ (-1.6±2.3)×10^{-17} year^{-1}. Uncertainty of this result includes the null result, indicating this constant may indeed be fundamental. Experiments have been proposed [2] that use transition frequencies of rovibrational states of the CaH^+ to search for variation of the proton-to-electron mass ratio β. Trapped atomic and molecular ions are also of interest to the astrochemistry community due their abundance in stellar atmospheres.

1.1   Using ion traps for precision measurements on molecular ions

Trapped ions are cooled using a technique called Doppler cooling. Although the ions are confined to a small space within the center of the trap, they still have some momentum. Ions are cooled using a laser with a frequency that is slightly shifted below the excitation frequency between the ground state and the first excited state of the ion. Ions moving towards the laser beam "see" the exact frequency needed for a transition, absorb a photon, and lose momentum. This yields an excited state that eventually decays, emitting another photon of greater energy, and the ion experiences a net loss in kinetic energy. Repeated interactions between the ions and the laser light leads to a dramatic cooling effect. This cooling process continues as long as the ions remain in resonance with the frequency of the laser light.

Doppler cooling can cool ions to temperatures on the order of 10^{-3}K. Ions become extremely localized at these low temperatures, allowing their spectra to be probed with excellent precision. The linewidths within the spectra are greatly reduced because they move at low velocities. [3] Cooled ions condense to form a Coulomb crystal, a three dimensional lattice of cold charged particles. The Coulomb repulsion between each ion within the crystal leads to separation distances on the order of microns. This novel state of matter can be stored for an extended period of time for study.

A possible first experiment to be performed in the Ion Trapping Lab will study the reaction between calcium ions and a neutral diatomic gas. Neutral diatomic hydrogen, H_2, will be leaked into the vacuum chamber and interact with the cooled calcium ions, $^{40}Ca^+$. The system will undergo a chemical reaction resulting in the formation of a diatomic molecular ion, CaH^+, and a neutral hydrogen atom, H

$$^{40}Ca^+ + H_2 \longrightarrow {}^{40}CaH^+ + H \tag{1.1}$$

The molecular ions formed are sympathetically cooled by the remaining laser cooled atomic ions. These ionic molecules are no longer in resonance with the cooling lasers used for the calcium ions; they do not fluoresce and cannot be imaged with the CCD camera. However, the number of molecular ions formed can be deduced by measuring the size of the crystal of atomic ions after the reaction.

1.2 Status of calculations on transitions in diatomic molecules

Ab initio calculations performed for neutral diatomic molecules outnumber those performed for ionic systems. Calculations for neutral alkali and alkaline-earth hydrides have been performed using a variety of methods. [4, 5, 6] Properties such as ionization energy, well depth, electron densities, etc. can be predicted using results from these calculations.

Results of calculations performed for diatomic molecular ions can predict the energy of the ground and excited electronic and vibrational states. Transitions between these states can be experimentally probed using spectroscopic techniques. Potential energy surfaces of the ground and excited states for several alkaline earth hydride molecular ions were generated by Aymar et al. [7] Calculations performed by Abe et al. [8] and Habli et al. [9] generated potential energy surfaces of ground and excited states of the CaH^+ molecular ion.

This work discusses three contributions to experiments on atomic and molecular ions in the Ion Trapping Lab. Chapter 2 is a discussion of the methods used to generate the potential energy surface of the CaH^+ molecular ion. These results were compared with previous calculations conducted on CaH^+. [8, 9] Chapter 3 gives a detailed review of the design and construction process of an ultra-high vacuum (UHV) compatible oven apparatus. This oven will be used to create a beam of neutral calcium vapor for ionization and trapping. Chapter 4 outlines the steps taken to construct a stable high voltage source to drive a lead zirconate titanate (PZT) crystal. This circuit allows the frequency of three lasers in the Ion Trapping Lab to be precisely tuned. A PID system will be used in conjunction with the circuit to ensure the frequency of each laser remains stable when subjected to external fluctuations. Test results using the final assembly are also given.

Chapter 2

Potential energy surfaces of CaH$^+$

2.1 Review of methods

This chapter presents calculations of the potential energy surface of the CaH$^+$ molecule. There are many programs dedicated to *ab initio* quantum chemistry simulations. Gaussian 09 [10] and NWChem [11] were used to perform the calculations within this chapter. These programs utilize a variety of methods and basis sets to predict properties of atoms and molecules.

Within the framework of quantum mechanics, the wave function Ψ of a system contains all information about the system. The wave function Ψ is an eigenfunction of the Schrödinger equation

$$\hat{H}\Psi = E\Psi \tag{2.1}$$

where $\hat{H}$ is the Hamiltonian operator and E is the energy eigenvalue of the system. The solutions yield the total energy of the system, i.e. of all electrons and nuclei. An appropriate Hamiltonian must be formulated that accurately describes the energy of the system. The non-relativistic Hamiltonian for a system with N electrons and M nuclei is

$$\hat{H} = -\sum_{i=1}^{N}\frac{\hbar^2}{2m}\nabla_i^2 - \sum_{a=1}^{M}\frac{\hbar^2}{2M_a}\nabla_a^2 - \sum_{i=1}^{N}\sum_{a=1}^{M}\frac{Z_a}{r_{ia}} + \sum_{i=1}^{N}\sum_{j>i}^{N}\frac{1}{r_{ij}} + \sum_{a=1}^{M}\sum_{b>a}^{M}\frac{Z_aZ_b}{R_{ab}} \tag{2.2}$$

where the first two terms are the kinetic energies of the electrons and nuclei, respectively, the third term is the Coulomb attraction between the electrons and nuclei, the fourth term is the interaction between electrons, and the last term is the interaction between nuclei. Exact solutions are only possible for one-electron systems, thus approximations must be made for two- or more electron systems.

One vital approximation is the Born-Oppenheimer approximation. This approximation allows the total wave function to be written as a product of the electronic and nuclear

components ψ_{elec} and ψ_{nuc}, respectively such that

$$\Psi(\mathbf{r}, \mathbf{R}) = \psi_{elec}(\mathbf{r}; \mathbf{R})\psi_{nuc}(\mathbf{R}) \tag{2.3}$$

The variables $\mathbf{r}$ and $\mathbf{R}$ are vectors that describe the coordinates of the electrons and nuclei, respectively. The Born-Oppenheimer approximation allows the nuclear coordinates $\mathbf{R}$ to be used as a parameter for the geometry of the system. As a result, the last term in equation 2.2 yields a constant at each geometry when applied to the total wave function. The electronic Hamiltonian H_{elec} is written as

$$\hat{H}_{elec} = -\sum_{i=1}^{N} \frac{\hbar^2}{2m} \nabla_i^2 - \sum_{i=1}^{N}\sum_{A=1}^{M} \frac{Z_A}{r_{iA}} + \sum_{i=1}^{N}\sum_{j>i}^{N} \frac{1}{r_{ij}} \tag{2.4}$$

and when applied to the electronic wave function ψ_{elec} the electronic Schrödinger equation

$$\hat{H}_{elec}\psi_{elec} = E_{elec}\psi_{elec} \tag{2.5}$$

yields the total electronic energy of the system at a particular geometry. A potential energy surface is generated by solving equation 2.5 for many geometries.

Now that an approximate Hamiltonian has been found, a suitable wave function describing the system should be formulated. In an atom, the electrons' spatial wave functions are characterized by radial and angular functions. The angular functions are dependent on the angular orbital quantum number l and its projection m and are described by spherical harmonic functions

$$\chi(\mathbf{r}) = R_{nl}(r)Y_{lm}(\theta, \phi) \tag{2.6}$$

where $\mathbf{r}$ parameterizes the spatial position of the electron. A linear combination of atomic orbitals (LCAO) is used to describe the molecular orbitals. Each molecular orbital is the sum

$$\phi_i(\mathbf{r}) = \sum_{j=1}^{N} c_{ji}\chi_j \tag{2.7}$$

A molecular spin orbital ψ_i is formed by introducing the spin of electrons

$$\begin{aligned} \psi_i(\mathbf{x}) &= \phi_i\alpha(\omega) \\ \psi_i(\mathbf{x}) &= \phi_i\beta(\omega) \end{aligned} \tag{2.8}$$

where $\alpha(\omega)$ and $\beta(\omega)$ represent spin-up or spin-down functions, respectively. The variable $\mathbf{x}$ parameterizes both the spatial position and the spin of the electron and is known as the electronic coordinate.

Because electrons are indistinguishable fermions, the wave function describing the system must be anti-symmetric. This means that if the position of two electrons are

interchanged the resulting wave function is the negative of the original wave function. The total wave function describing the system is realized by a Slater determinant. For an N-electron system, the wave function can be written as

$$\Psi(\mathbf{x}_1, \mathbf{x}_2, \ldots, \mathbf{x}_N) = \frac{1}{\sqrt{N!}} \begin{vmatrix} \psi_i(\mathbf{x}_1) & \psi_j(\mathbf{x}_1) & \cdots & \psi_k(\mathbf{x}_1) \\ \psi_i(\mathbf{x}_2) & \psi_j(\mathbf{x}_2) & \cdots & \psi_k(\mathbf{x}_2) \\ \vdots & \vdots & \ddots & \vdots \\ \psi_i(\mathbf{x}_N) & \psi_j(\mathbf{x}_N) & \cdots & \psi_k(\mathbf{x}_N) \end{vmatrix} \tag{2.9}$$

A Slater determinant considers all molecular spin orbitals and satisfies the anti-symmetric property of the total wave function. Interchanging two rows of the determinant changes the sign of the systems wave function, satisfying the anti-symmetric property. If two rows are equal the determinant becomes zero, satisfying the Pauli exclusion principle.

Hartree-Fock method

The Hartree-Fock (HF) method [12, 13] is the simplest *ab initio* method and is usually the first method employed in quantum chemistry calculations. This variational method provides an upper bound of the electronic energy of the system by applying the self-consistent-field (SCF) procedure.

An initial guess at the molecular orbitals is used to calculate the mean-field. A new set of molecular orbitals is computed by applying the Fock operator to the initial guess. The procedure is repeated until the field no longer changes and the molecular orbitals are eigenfunctions of the Fock operator. The molecular orbitals with the lowest energy are called occupied molecular orbitals and are occupied by the N electrons. The remaining molecular orbitals are called virtual molecular orbitals. The optimal molecular orbitals ϕ_i are given by the Fock equation

$$\hat{f}_i \phi_i = \varepsilon_i \phi_i \tag{2.10}$$

where f_i is the Fock operator and

$$\hat{f}_i = -\frac{1}{2}\nabla_i^2 - \sum_{A=1}^{M} \frac{Z_A}{r_{iA}} + \sum_j \left\{ 2\hat{J}_j - \hat{K}_j \right\} \tag{2.11}$$

The first two terms describe the kinetic energy of the ith electron and its Coulomb interaction with any nuclei, respectively. The last two terms describe the mean-field affecting the ith electron and are the Coulomb and exchange operators, respectively. Each operator is applied to a molecular orbital ϕ_i yielding

$$\hat{J}_j \phi_i(\mathbf{r}_1) = \phi_i(\mathbf{r}_1) \int \phi_j^*(\mathbf{r}_1) \frac{1}{|\mathbf{r}_1 - \mathbf{r}_2|} \phi_j(\mathbf{r}_2) d\mathbf{r}_1$$

$$\hat{K}_j \phi_i(\mathbf{r}_1) = \phi_j(\mathbf{r}_1) \int \phi_j^*(\mathbf{r}_1) \frac{1}{|\mathbf{r}_1 - \mathbf{r}_2|} \phi_i(\mathbf{r}_2) d\mathbf{r}_2 \tag{2.12}$$

and describe the effect of the Coulomb interaction between electrons and exchanging electrons' positions, respectively.

An infinite set of terms in equation 2.7 is required to achieve the exact electronic energy. A basis set approximation is made to expand this sum using a finite set of known functions. The Fock equation is then applied using this basis set expansion

$$\hat{f}_i \sum_j^K c_{ji}\chi_j = \varepsilon_i \sum_j^K c_{ji}\chi_j \tag{2.13}$$

where C_{ij} is a matrix of coefficients and K is the number of functions used in the basis set. Adopting the common bra-ket notation to represent each atomic spin orbital

$$\chi_j \equiv |\chi_j\rangle \qquad \chi_j^* \equiv \langle\chi_j| \tag{2.14}$$

and taking the inner product of equation 2.13 yields the Roothan-Hall equation [14]

$$\mathbf{FC} = \mathbf{SC}\boldsymbol{\varepsilon} \tag{2.15}$$

where $\mathbf{F}$ represents the Fock matrix, $\mathbf{C}$ represents a matrix of atomic orbital expansion coefficients, $\mathbf{S}$ represent the overlap matrix, and $\boldsymbol{\varepsilon}$ represents a matrix that contains the energy eigenvalues. Individual elements within $\mathbf{F}$ and $\mathbf{S}$ are found by taking the inner products

$$\begin{aligned} F_{jk} &= \langle\chi_j|\hat{f}|\chi_k\rangle \\ S_{jk} &= \langle\chi_j|\chi_k\rangle \end{aligned} \tag{2.16}$$

After the SCF procedure is completed, the resulting coefficient matrix minimizes the energy for a given basis set.

The correlation energy of electrons is not included in the HF method. Instead, the interaction between an electron and the average electric field resulting from all other electrons is calculated. Several post-HF methods used to include correlation between electrons resulting from their constant motion. The methods used for this work were CCSD and CCSD(T).

Coupled-cluster methods

Coupled-cluster methods [15, 16] account for the correlation between electrons. Correlation is an important factor for both atoms and molecules. These methods are size-consistent, meaning that when applied to a system of isolated molecules, the method provides the sum of the resulting energies when the method is applied to each molecule. Total energy of the system including correlation energy is

$$E_{tot} = E_{HF} + E_{corr} \tag{2.17}$$

where E_{HF} and E_{corr} are the energies found using the HF method and the correlation energy, respectively. Like the HF method, this procedure is performed iteratively however the calculated energy may not be lowered by subsequent iterations.

Coupled-cluster methods define an excitation operator $\hat{T}$

$$\hat{T} = \hat{T}_1 + \hat{T}_2 + \hat{T}_3 + \cdots + \hat{T}_{N_{elec}} \tag{2.18}$$

that acts of the HF determined wave function Ψ_{HF} such that

$$|\Psi_{CC}\rangle = e^{\hat{T}}|\Psi_{HF}\rangle \tag{2.19}$$

This definition prohibits the variational method from being employed. A Taylor series of the exponential can be used to show which operators will appear compared to applying the operator $\hat{T}$ to the wave function.

$$\sum_{k=0}^{\infty} \frac{1}{k!}\hat{T}^k = \hat{1} + \hat{T} + \frac{1}{2}\hat{T}^2 + \frac{1}{6}\hat{T}^3 + \cdots \tag{2.20}$$

The Schrödinger equation for coupled-cluster methods becomes

$$\hat{H}\left(e^{\hat{T}}|\Psi_{HF}\rangle\right) = E\left(e^{\hat{T}}|\Psi_{HF}\rangle\right) = E_{CC}|\Psi_{CC}\rangle \tag{2.21}$$

where E_{CC} is the coupled-cluster energy. This is found by taking the inner product with the HF wave function

$$E_{CC} = \langle\Psi_{HF}|\hat{H}|\Psi_{CC}\rangle \tag{2.22}$$

Including additional terms in equation 2.18 accounts for more excitations and may lead to a more accurate potential energy curve. Additional excitations included will significantly increase the resources and time required for a calculation.

The following letters, after CC, indicate the number of excitations between occupied and virtual orbitals. For CCSD, the coupled-cluster wave function is defined that account for single and double excitations

$$|\Psi_{CC}\rangle = e^{\hat{T}_1+\hat{T}_2}|\Psi_{HF}\rangle \tag{2.23}$$

CCSD(T) uses the same wave function but also treats triple substitutions as a perturbation. Calculations for this work started at the CCSD level of theory. These results were improved upon by increasing the level of theory to CCSD(T).

Basis sets

The calculations performed for this work used the correlation consistent basis sets cc-pVXZ [17, 18], where the X corresponds to the size of the basis set used.

These basis sets are composed of functions that describe correlation effects. Each subsequent basis set adds additional correlating functions to describe valence orbitals to the minimal basis set required to describe an atom, leading to a small reduction in calculated energy. For example, the double-zeta (DZ) basis set adds correlating functions to describe two additional valence orbitals. The cc-pCVXZ [17] basis sets were also used for the calcium atom. These are basis sets that are composed of correlating functions that describe core orbitals in addition to those to describe the valence orbitals included.

2.2 Results of CaH$^+$ calculations

Several simulations of the CaH$^+$ molecular ion were conducted. All calculations were performed using the Palmetto Cluster. Multiple potential energy surfaces were generated for the ground state of the CaH$^+$ molecular ion.

Calculations were first performed using Gaussian 09 at the CCSD level of theory. Post-HF method freeze the core orbitals of the system by default. Correlation energy for electrons occupying these frozen orbitals is not calculated. All orbitals can be unfrozen by calling the "Full" option within the input file. Calculations at the CCSD level of theory were repeated to include all orbitals. The level of theory was increased to CCSD(T), which includes perturbative triple excitations non-iteratively. Calculations at this level of theory were performed for using frozen and unfrozen core orbitals. These calculations initially used the cc-pVDZ basis set. Subsequent calculations used increasingly larger basis sets, up to cc-pV5Z.

NWChem was also used to perform calculations at the CCSD(T) level of theory. Polarized functions were added the the core orbitals of the calcium atom using the cc-pCVXZ basis sets. The hydrogen atom used the cc-pVXZ basis sets. These calculations initially used the cc-pCVDZ and cc-pVDZ basis sets for the calcium and hydrogen atoms, respectively. Subsequent calculations used increasingly larger basis sets, up to cc-pCVQZ and cc-pVQZ basis sets for the calcium and hydrogen atoms, respectively. The cardinal number of the basis set used for each atom was identical for each calculation.

The SCF energy for the cc-pVDZ basis set was subtracted from the SCF energy from larger basis sets. A power law [19] was fitted to the three points plotted in figure 2.1. The power law used was

$$Y(x) = Y_{CBS} + Ax^{-3} \tag{2.24}$$

where Y_{CBS} is the extrapolated value for the infinite basis set, A is a fitting constant, and x is the cardinal number of the basis set used. Table 2.1 summarizes the values calculated for each geometry.

geometry	Y_{CBS} [a.u.]	A
R = 1.9Å	-0.013547	0.056953
R = 8.0Å	-0.012234	0.050210

Table 2.1: Calculated values to fit the plotted points using equation 2.2. The calculated values of Y_{CBS} for each geometry are plotted as dashed lines in figure 2.1

Figure 2.1 shows that the SCF energy approaches the extrapolated limit Y_{CBS} as the cardinal number increases.
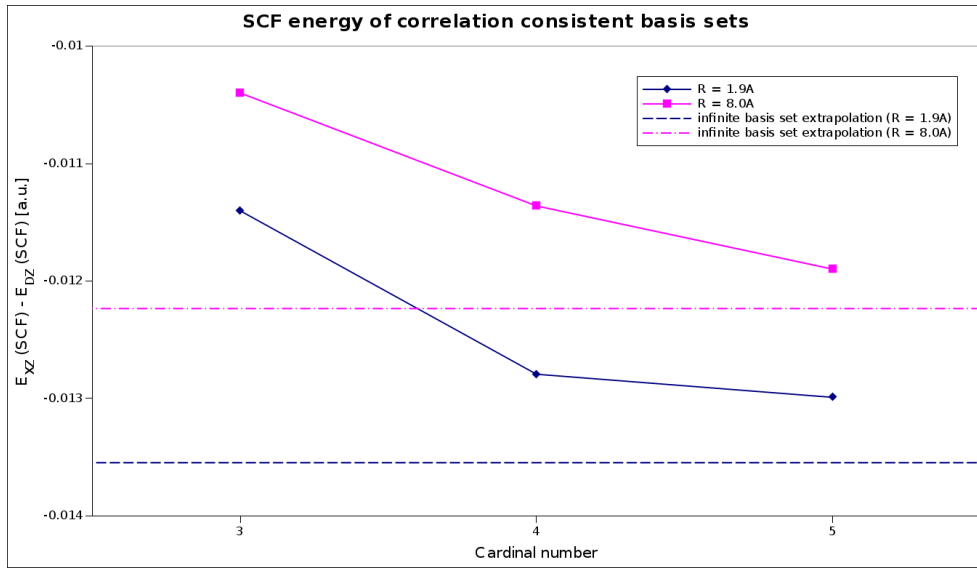
Figure 2.1: The relative difference of ground state SCF energy of the CaH$^+$ molecular ion as a function of cardinal number of the basis set for two selected geometries, R = 1.9Åand R = 8.0Å. Horizontal dashed lines represent the SCF energy extrapolated for an infinite basis set at each geometry.

Correlation energy for a particular geometry was calculated using the SCF energy and the CCSD or CCSD(T) energy

$$
\begin{aligned}
E_X^{corr} &= E_X^{CCSD} - E_X^{SCF} \\
E_X^{corr} &= E_X^{CCSD(T)} - E_X^{SCF}
\end{aligned}
\tag{2.25}
$$

Extrapolated correlation energy for an infinite basis set was calculated using the correlation energies of two basis sets [20]

$$
E_{XY}^{\infty} = \frac{E_X^{corr}X^3 - E_Y^{corr}Y^3}{X^3 - Y^3}
\tag{2.26}
$$

where X and Y are the cardinal numbers of two sequential basis sets, E_X^{corr} and E_Y^{corr} are the correlation energies calculating using each basis set, and E_{XY}^{∞} is the extrapolated value. Extrapolated correlation energy for two geometries are shown in table 2.2. Figures 2.2 and 2.3 show that the correlation energy at both levels of theory

geometry	CCSD corr. [a.u.]	CCSD(T) corr. [a.u.]
R = 1.9Å	-0.361049	-0.371111
R = 8.0Å	-0.479124	-0.510618

Table 2.2: Extrapolated correlation energies for an infinite basis set is calculated using equation 2.26. These values are plotted as dashed lines in figures 2.2 and 2.3.

approach the extrapolated value as the cardinal number increases for each geometry. As larger basis sets are used, the correlation energy is expected to approach the extrapolated value. The difference in y-values between each of the points in figures 2.2 and 2.3 becomes smaller for larger cardinal numbers.
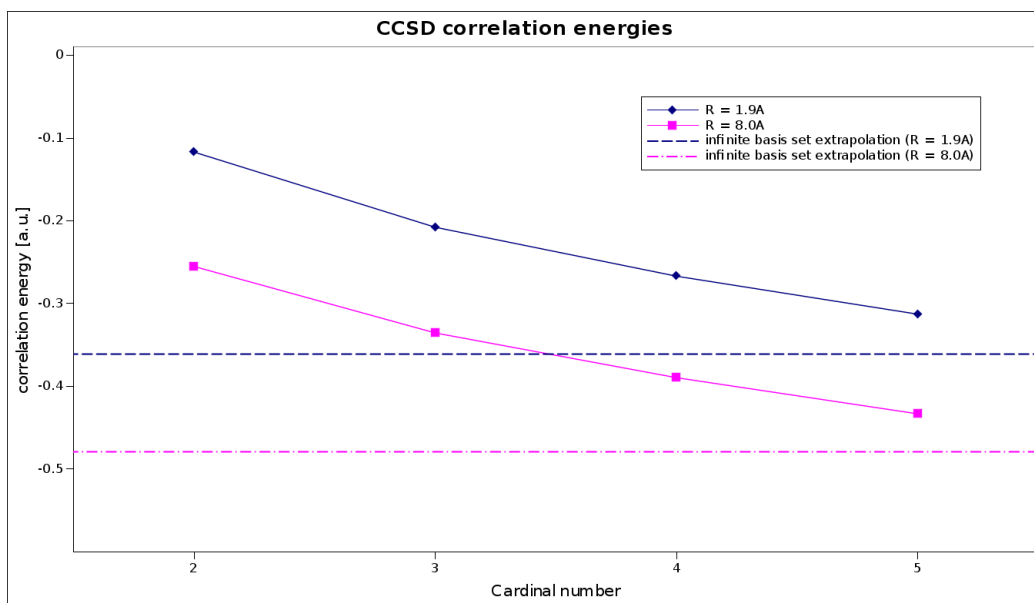
Figure 2.2: The correction to the HF energies accounting for electron correlation as a function of cardinal number of the basis set for two selected geometries, R = 1.9Åand R = 8.0Åusing the CCSD method. The horizontal dashed lines represent the correlation energy extrapolated for an infinite basis set at each geometry.

Equation 2.26 was applied at each geometry using the CCSD(T) correlation energy of the cc-pVQZ and cc-pV5Z basis sets for the ground state. This value was then added to the SCF energy calculated for the cc-pV5Z basis set. This yields the extrapolated energy for an infinite basis set at each geometry

$$E^{\infty}(R) = E_{SCF}^{5Z}(R) + E_{CCSD(T)}^{\infty}(R) \tag{2.27}$$
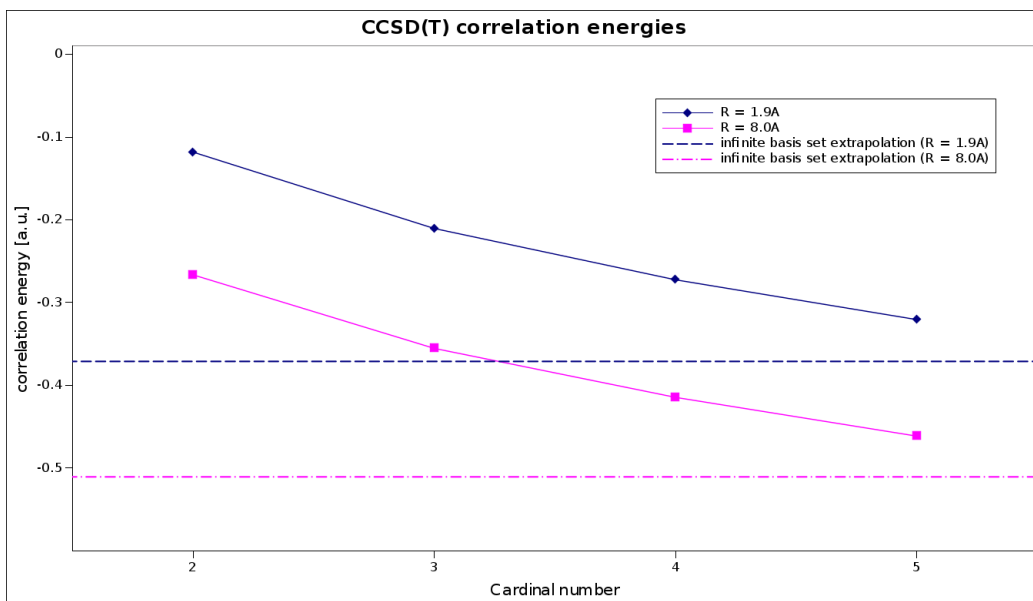
Figure 2.3: The correction to the HF energies accounting for electron correlation as a function of cardinal number of the basis set for two selected geometries, R = 1.9Åand R = 8.0Åusing the CCSD(T) method. The horizontal dashed lines represent the correlation energy extrapolated for an infinite basis set at each geometry.

at the CCSD(T) level of theory. Figure 2.4 shows that including the extrapolation for an infinite basis set results in a lower energy at each geometry. Another noteworthy feature of the ground state potential is the positive potential barrier at geometries R>3.65Å. This barrier is present when perturbations for triple substitutions are accounted for using the CCSD(T) method. The presence of this barrier implies that energy is required to form the CaH^+ molecule at the CCSD(T) level of theory.

The effect of adding polarization to the core orbitals of the calcium atom on the potential energy surface can be seen in figure 2.5. The addition of polarized core orbitals to the calcium atom lowered the energy for geometries between R = 1.05Åand R = 1.60Å. The molecule is more stable at these geometries when polarization is added to the core orbitals of the calcium.
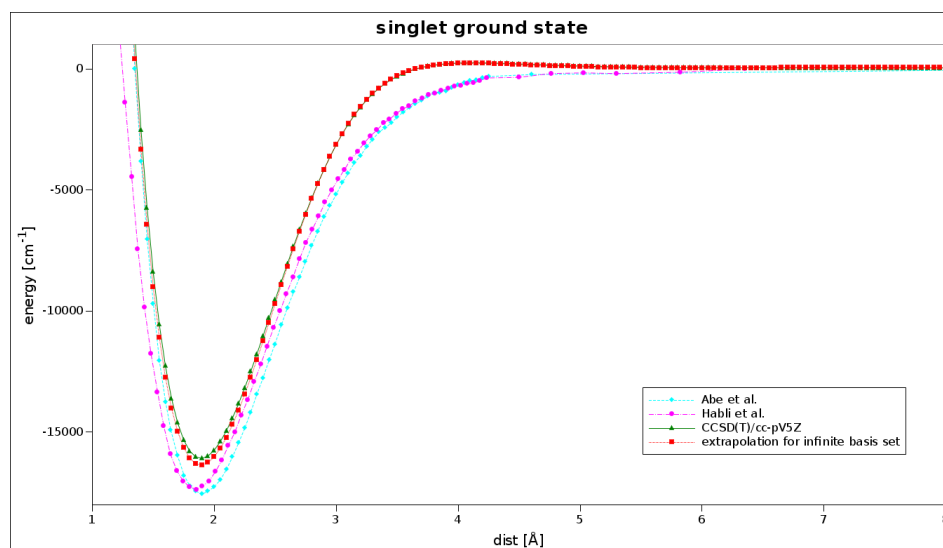
Figure 2.4: The potential energy surface of the singlet ground state of the CaH$^+$ molecular ion using the CCSD(T) method. The curve of green triangles uses the cc-pV5Z basis set. The curve of red squares includes the correlation energy extrapolated for an infinite basis set at each geometry. Also plotted are previous calculations from Abe et al. [8] and Habli et al. [9]
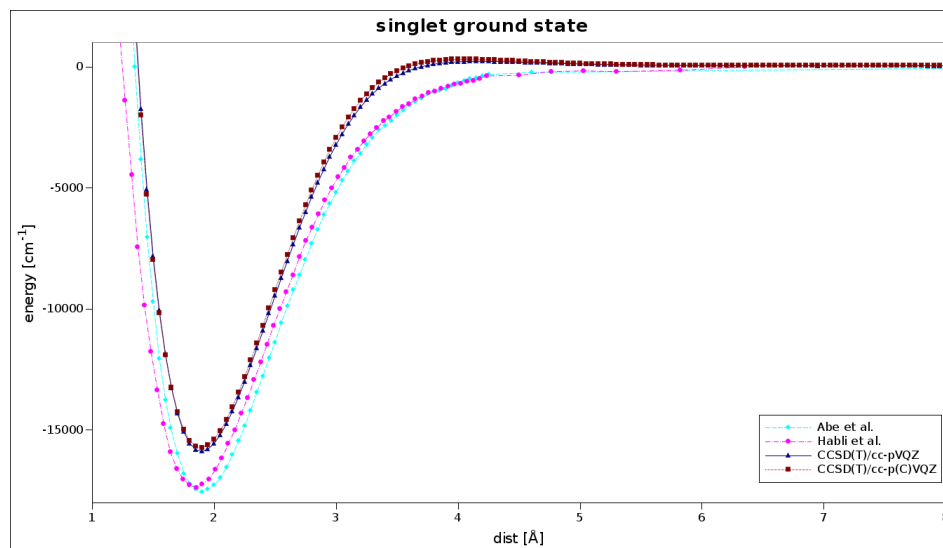
Figure 2.5: The potential energy surface of the singlet ground state of the CaH$^+$ molecular ion using the CCSD(T) method. The curve of red squares corresponds to the cc-pVQZ basis set used for both atoms. The curve of blue triangles corresponds to the cc-pCVQZ and cc-pVQZ basis set used on the calcium and hydrogen atoms, respectively. Also plotted are previous calculations from Abe et al. [8] and Habli et al. [9]

13

Chapter 3

UHV compatible calcium oven

A beam of neutral calcium vapor is required to form ionized calcium in the trap center. This is accomplished through the use of an ultra-high vacuum (UHV) compatible oven that can reach the vaporization temperature of calcium. Pressures within the chamber are on the order of 10^{-9} torr. All components of the assembly must be fabricated using materials that do not outgas, which would adversely affect the desired chamber pressure. Calcium is ejected from the oven towards the trap center once the vaporization temperature is reached. This beam of calcium vapor then interacts with the ionization lasers.

3.1 Mechanical design

The design of the oven assembly was adapted from previous work [21] with calcium ions. The assembly consists of a MACOR® oven, plates securing the oven, one or more skimmer plates, and supporting rods screwed into the coaxial feedthrough flange. All plates, supporting rods, set screws/nuts, and the feedthrough flange were constructed of stainless steel.

The feedthrough flange is 2.75" conflat flange and has four BNC feedthroughs.[1] Four male BNC pins extend 0.36" from the internal face and are placed on a circle 0.425" in radius from the center of the flange. Two opposing holes were tapped for size 5-40 screws and placed on a circle 1.125" in diameter centered on the flange to mount the supporting rods. A later design called for holes placed on a circle 0.9" in diameter and tapped for 2-56 threaded rods. A rendering of the feedthrough flange is shown in figure 3.1.

---

[1] MDC 9212004
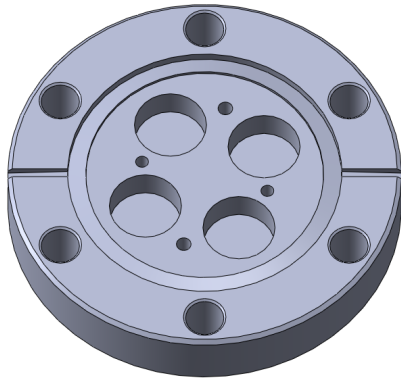
Figure 3.1: A rendering of the feedthrough flange with threaded holes for the supporting rods. Not pictured are the BNC pins that extend from the center of the four symmetrically placed recesses.
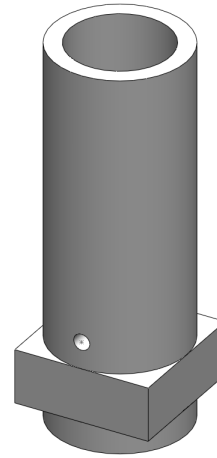
Figure 3.2: A rendering of the MACOR® oven that was used to vaporize calcium. Thermocouple wire was fed through the small opening near the bottom. Tungsten filament was then wound around the circular portion.

Originally, the oven was designed as a partially hollow rectangular prism 0.25" long by 0.25" wide by 0.75" deep. A 0.1875" diameter hole was drilled 0.625" along its center axis to provide space for solid calcium. Two small holes were drilled into opposite faces 0.6" from the open end, perpendicular to the central axis, for thermocouple wires. This design proved impractical during assembly because tungsten filament could not be easily wound around its flat faces. A new design was fabricated by shaving the square edges to form a cylinder 0.25" in diameter. The hollow portion and holes through two of the faces were unaffected. A small portion of the oven retained its flat faces to secure the oven into place during assembly.

Three designs of the supporting rods were fabricated over the course of testing. The initial design was a 0.125" diameter rod 3" in length. The bottom 0.2" of the rods were threaded to screw into the tapped holes on the internal face of the feedthrough flange. Each rod was beveled on the outward-facing side to position and secure the mounting and skimmer plates with set screws. It was noted that air could be trapped when the rods were screwed into the flange, creating a virtual leak as the air escaped into the test chamber once under vacuum. Small notches were cut from the threaded portion of the rods to solve this problem. The second design was similar to the first except the lower portion of the rod had a larger radius (see figure 3.3).This prevented shorting between the BNC connectors and the assembly. As before, the bottom 0.2" was threaded to screw into the internal face of the flange. The thicker portion of the

rod was 0.25" in diameter and extended 0.75" in length. The rest of the rod was 0.125" in diameter, extended 1.75" in length, and was beveled on the outward-facing side. To prevent virtual leaks, a small hole was drilled into the bottom of the rod along its central axis which intersected another small hole drilled radially into the rod. The third design used 2-56 threaded rods. This design used nuts to position and secure each plate.
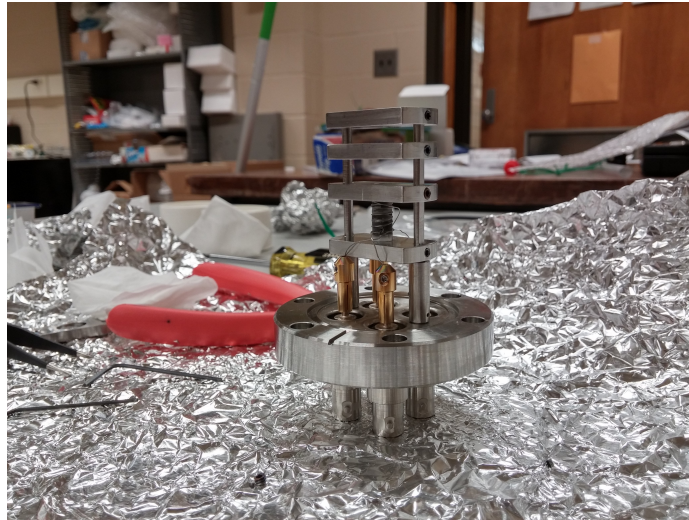
Figure 3.3: This assembly uses the second design of supporting rods and plates. The supporting rods extend 2.5" from the inside face of the feedthrough flange.

Design of the plates were dependent upon the design of both the oven and the supporting rods. The first and second set of plates were designed to use set screws for positioning along the rods. The rods fit through two through-holes 0.13" in diameter placed near the edges of each plate. Distance between these holes was governed by the distance (1.125") between the two rods. Each plate utilizing size 2-56 set screws was 0.68" wide and 1.36" long with rounded edges with enough clearance to fit into the test chamber. Thickness of the first set of plates was 0.125" but was later changed to 0.187" so larger, size 4-40 set screws, could be used. Two holes were drilled into either side of each plate to intersect the through-holes and were threaded for set screws. A third plate design was created due to clearance issues of previous designs. Set screws used in the previous designs would make contact with the inner walls of the test chamber. Installing the apparatus within the chamber for testing proved troublesome and could potentially alter the position of the plates. The third set of plates utilized the size 2-56 threaded rods and were smaller in area than previous designs. Each of these plates was 0.55" wide and 1.10" long with two through holes for the threaded rods. Additionally, these plates were 0.048" thick, thinner than the previous two designs.

Each design consisted of two oven mounting plates and one or more skimmer

plates. The first bottom mounting plate was designed with a recessed square inset 0.05" deep to hold the bottom of the oven in place. Subsequent designs used a circular inset to match the cylindrical oven design. The original top mounting plate had a 0.17" diameter through-hole positioned at its center, acting as a collar for the oven. When a thicker plate was designed, a 0.25" through-hole was placed at the center of the plate. This hole provided clearance for the oven and acted as a collar to secure the top. The third design used the smaller and thinner plates, each with a 0.25" diameter hole placed at the center.

Skimmer plates were designed to block a portion of the vapor beam as it exited the oven. The first skimmer design was a 0.25" thick plate with a single through-hole 0.04" in diameter placed at the center of a plate. The second skimmer plate design used two skimmers to narrow the beam. Each of these 0.5" thick skimmers were designed with horizontal or vertical openings 0.04" wide centered on the plate. These openings blocked atoms with high horizontal or vertical exit velocities from the oven. A third design reverted back to a circular opening 0.04" in diameter placed at the center of a 0.125" thick plate.

3.2   Procedure

Each component of the assembly was thoroughly cleaned after fabrication to meet UHV requirements. Assembly began by threading two thermocouple wires [2] through the openings on either side of the oven. A portion of the wires were pulled out of the open end of the oven using forceps and twisted together. Free ends of each wire were gently pulled back out of the openings to position the twisted portion at the bottom of the oven. Tungsten filament[3] 0.005" in diameter was tightly wound around a clean screwdriver 0.1875" in diameter. A single loop of filament was placed around the open end of the oven. More loops were wound around the oven by twisting the entire looped portion, effectively screwing it into place. Since the loop diameter was slightly less than the oven diameter, the filament hugged the walls of the oven.

Supporting rods were screwed into the feedthrough flange and the lower mounting plate was placed slightly above the brass fittings.[4] The wired oven was physically secured between the upper and lower mounting plates. Each wire was threaded into the brass fittings and secured to the pin with set screws after any excess length was removed. Forceps were used to re-position the wires to prevent shorts with the structure and themselves. One or more skimmer plates were then placed onto the rods above the mounting plates, completing the assembly. Distance between each

---

[2] Omega, SPCH-015-50 Chromega® E positive
    Omega, SPCI-010-50 Constantan E negative
[3] ESPI metals, 3N8 purity
[4] MDC 9924003

pair of plates was measured and the number of filament loops around the oven was recorded.

The calcium pellets[5] provided were sealed in a glass vial filled with argon that prevented oxidation. Once exposed to atmosphere, neutral calcium oxidizes and forms a crust of calcium oxide on the outer layer of the pellets. This crust hinders vaporization of the neutral calcium underneath because its vaporization temperature is significantly higher. A blade could be used to scrape this brittle layer from the surface but could not be removed entirely. Any calcium that underwent significant oxidation was discarded.

A glove bag was used to load the calcium into the oven. The sealed vial of solid calcium, oven assembly, forceps, and wire cutters were placed into the glove bag. Pressurized nitrogen was then leaked into the partially sealed glove bag, flushing it of atmosphere. After approximately five minutes, the glove bag was completely sealed and allowed to inflate with nitrogen. The sealed glass vial was broken by striking the top with a hammer from outside of the glove bag. At this time, the calcium would begin to oxidize, although at a very slow rate due to the low amount of oxygen present within the glove bag.

Calcium is a relatively soft metal and can be cut using wire cutters. The pellets were cut into many small pieces (< 0.5cm) to be loaded. By cutting the pellets into many small pieces, the amount of surface area exposed to the high temperature is maximized. Smaller pieces were also easier to load into the oven opening. Pieces were dropped into the oven using the forceps until it was approximately two-thirds full. Knowing that the oven would be positioned horizontally during testing, the pieces were gently packed down to reduce the likelihood of any pieces falling out during installation into the chamber.

The glove bag was then opened and the oven assembly was quickly brought to the testing chamber. It was found that the set screws would sometimes make contact with the inner wall of the test chamber. By slightly rotating the assembly as it was slid into the chamber, contact with the inner wall could sometimes be avoided. The third plate design alleviated this problem by avoiding the use of set screws. The vacuum pump system was turned on to pump atmosphere from the chamber. After the pressure within the chamber equilibrated, a test could begin.

An adjustable high current supply was connected to the coaxial ports corresponding to each end of the tungsten filament. The vacuum gauge and thermocouple leads were connected to a computer via coaxial cables. A LABVIEW® program was used to record the oven temperature and pressure within the chamber. A baseline measurement of temperature and pressure were recorded with the oven turned off. The current supplied to the filament was then increased in steps of 0.5A. After thermal equilibration the voltage, temperature, and pressure were recorded by hand. As the

---

[5] ESPI metals, 3N purity

temperature approached 600°C, the interior of the chamber was visually inspected for debris. If there was no evidence of debris, the current was increased and the test continued.

3.3   Results

For the results discussed in this chapter, chamber pressures ranged from 10^{-1} to below 10^{-4} torr and oven temperatures ranged from room temperature to over 1000°C. The tests were conducted in a 6-arm vacuum chamber mounted onto an optical table. Three of these arms were sealed with blank flanges while the others were used for the oven assembly, connection to vacuum system, and a viewport. Deposition of calcium vapor was to be observed on the inner side of the viewport. This would provide a qualitative measurement of vaporization and an estimation of the temperature needed to vaporize the calcium sample.
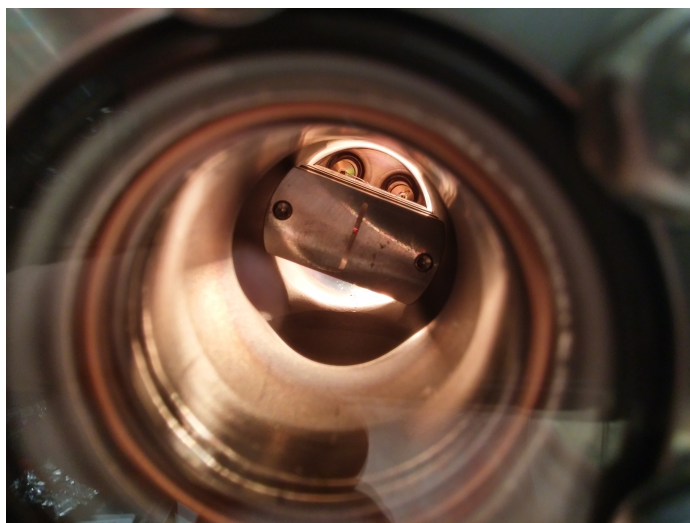
Figure 3.4: A view inside the chamber while a test is being conducted. The interior is lit by the tungsten filament, similar to an incandescent light bulb. Temperatures within the oven can exceed 1000°C.

Test results were inconclusive for several trials. Previous work showed that calcium undergoes vaporization at approximately 600°C under UHV. Initially, the turbopump was unavailable and a rough pump was used to reach and sustain pressures ranging from 0.1 to 0.01 torr. Although the oven temperature reached 600°C during these trials, no debris accumulated on the window. During one trial temperatures surpassed 1000°C, the maximum stable temperature for MACOR® which resulted in irreparable damage to the oven. An identical oven was fabricated and tests were continued using this replacement. The oven assembly was removed after each trial. After disassembly,

each component was inspected for evidence of vaporization, specifically the skimmer plates. Any damaged components were replaced during reassembly for a following trial. The tungsten filament and the thermocouple wires were usually replaced after each trial due to degradation. Both were often extremely brittle and would break under very small amounts of stress.

Debris was observed on the skimmer plates after many trials once it was exposed to atmosphere and oxidized. This indicated that calcium was being vaporized but something was preventing the vapor from reaching the view port. One possible reason was that after an extended period of time at or above the vaporization temperature, vapor condensed on the relatively colder plates, blocking the opening in the skimmer plates. This could be remedied by reducing the thickness of the skimmer plates. Thinner plates were designed and fabricated, reducing the chance of condensation. A second possibility was that the pressure within the chamber was too high. This would cause more collisions between background gas particles and the vapor, impeding its path. Multiple collisions can reduce the temperature of the vapor enough to cause condensation as well as dispersing the beam. Evidence of this was observed by a thin layer of calcium coating the inner walls of the chamber oxidized between trials. Lower pressures were reached when the turbopump was installed and used in conjunction with the rough pump. It was also possible that the path length between the oven and the inner side of the view port was too great. A thin glass slide was placed between turns of a coil. The glass slide was the positioned less than one inch from the front of the assembly to reduce the path length to the deposition site.

Evidence of vaporization was first observed at a temperature of 530°C and a pressure lower than 10^{-4} torr. The pressure gauge that was used could not read below this limit so the exact pressure within the chamber is unknown. The current supplied to the filament was 4.6A and was gradually increased to 5.8A, increasing the temperature to 610°C. This was sustained for approximately 4 hours and 20 minutes resulting in a calcium deposit 8.16mm in diameter onto the glass slide. The skimmer with a circular hole was used and a bulls-eye pattern was expected, with thicker deposits in the center and decreasing thickness further from the center. This was not observed as the deposit was thicker in one quadrant of the circle, indicating the hole may have become clogged during the trial.

Another successful trial was conducted with the vertical and horizontal skimmers. Current supplied to the filament was gradually increased to 3.8A yielding a temperature of approximately 620°C. Debris was immediately observed on the glass slide and the temperature was sustained for one hour. Material was deposited in an oval and the pattern was relatively homogeneous with thicker deposits near the center and decreasing thickness further from the center. The longitudinal diameter and latitudinal diameters were 6.14mm and 13.76mm respectively.

3.3.1 Temperature vs. current

Table 3.1 shows the data recorded for a single trial. This particular trial was the first trial evidence of debris on the glass slide was observed.

time elapsed [min.]	voltage [V]	current [A]	temperature [°C]
0	0	0	25
20	0.4	0.6	35
25	0.8	1.2	80
30	1.5	1.8	170
34	2.5	2.4	300
40	3.6	3.0	420
45*	4.6	3.6	530
105	5.8	4.0	610
225	5.7	4.0	610

Table 3.1: Data recorded for an oven test conducted on September 12, 2014. Debris was observed on the glass slide when the current flowing through the tungsten filament reached 3.6A. The measured temperature within the oven was 530°C.

3.3.2 Beam dispersion

Dispersion of the beam depends upon the total path length, geometry of the skimmer plates used, and the pressure within the vacuum chamber. The following analysis assumes that the oven is a point source of calcium vapor and the system is placed in a perfect vacuum.
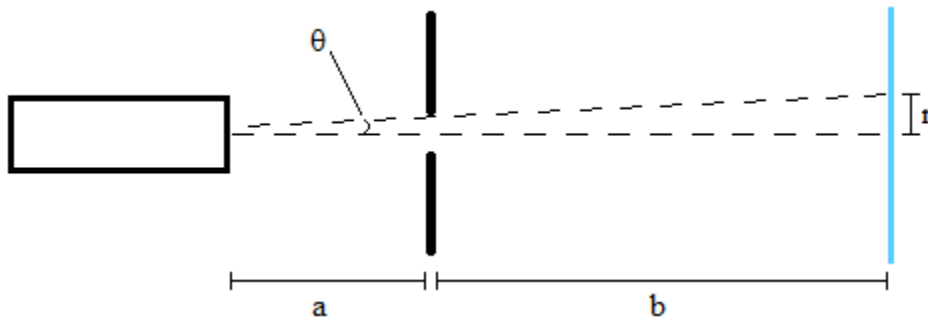

Figure 3.5: A simplified depiction of the configuration used to test the oven. Vaporized atoms with trajectories within the dashed lines are deposited onto the glass slide (light blue vertical line) after they exit the oven (black box). Note: distances are not not to scale.

The dispersion angle can be calculated using

$$\theta = \tan^{-1}\left(\frac{\delta/2}{a}\right) \tag{3.1}$$

where θ is the dispersion angle, δ is the size of the skimmer opening, and a is distance between the opening of the oven and the skimmer plate. The radius of the debris field formed on the glass slide can be calculated using the dispersion angle

$$r = (a + b + t)\tan\theta \tag{3.2}$$

where b is the distance between the skimmer plate and the glass slide and t is the thickness of the skimmer plate. If the path length is much larger than the skimmer plate thickness, i.e. $a + b \gg t$, t can be neglected in equation 3.2.

Evidence of deposition was first observed using a set up where $a = 0.53"$, $b = 0.79"$, and $\delta = 0.04"$. Equations 3.1 and 3.2 yield values of $\theta = 2.16°$ and $r = 0.05"$ for the beam dispersion angle and debris field radius. The measured radius of the debris field was $r = 0.15"$. This difference may be a consequence of the assumptions made about the experimental set up. Additional dispersion can be caused by collisions between vaporized atoms and background gas. Vaporized atoms do not exit the oven from a single point at the center of the opening. Neglecting the skimmer plate thickness can also contribute to this difference.

It is crucial that no vapor is deposited onto the trap electrodes, which could adversely affect the location of the ions within the trap. The debris field radius must be smaller than half the vertical distance between the trap electrodes.
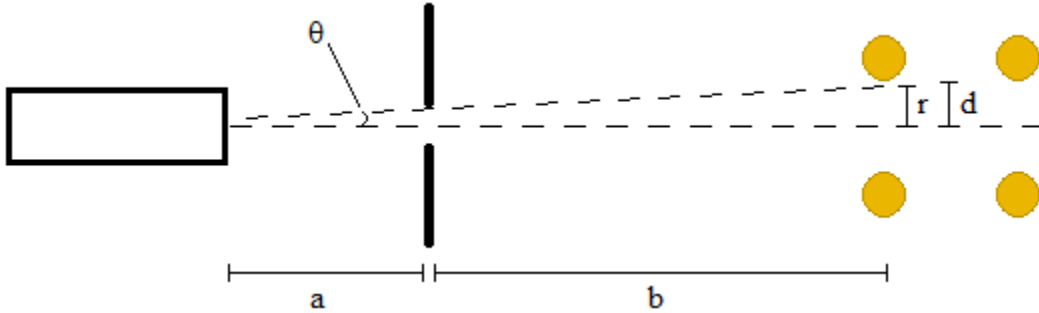
Figure 3.6: A simplified depiction of the current configuration within the vacuum chamber. Calcium vapor exits the oven and is focused by skimmer plates. Atoms with trajectories within the dashed lines pass through trap (yellow circles). Note: distances are not not to scale.

Distance between the oven opening and the skimmer plate was $a = 0.82"$, yielding a beam dispersion angle of 1.4°. The trap electrodes are located a distance $b = 1.7"$

from the skimmer plate. Calculated debris field radius for this configuration is $r = 0.06"$. The vertical distance between the trap electrodes and center of the trap is $d = 0.03"$, indicating that debris can potentially be deposited on the surface of the electrodes. Increasing the distance between the oven opening and the skimmer plate reduces the beam dispersion angle. This could reduce the amount of vapor deposited onto the electrode surfaces.

Chapter 4

Stable high voltage source for driving PZT

The wavelengths of the diode lasers used for Doppler cooling and spectroscopy must be extremely stable. Any deviation from a specific wavelength causes the laser to fall out of resonance with the excitation frequency of a transition. A diode laser uses light passing through a diffraction grating as feedback into the diode to emit light at a specific wavelength. Adjusting the angle of the diffraction grating changes the feedback to the diode, affecting the wavelength of light it emits. This angle is adjusted using PZT crystal placed behind the diffraction grating that intersects the path of the laser beam. Applying a voltage across the surface of these crystals changes their size by a very small amount. These crystals allow precise manipulation of the diffraction grating angle. The final design will be used with a PID to correct minute errors due to external fluctuations.

4.1   Electronic Design

The original design was adapted from previous work with external cavity diode lasers [22]. This design used an AD823AN[1] for the first amplifier whose output could range from 3V to 36V. It was powered by a dual supply with $V_- = -10V$ and $V_+ = 12V$. The AD823AN was connected in an inverting configuration. A design using an AMP03[2] amplifier was also constructed. The AMP03 amplifier was used because its output is extremely stable. It was set up in an inverting configuration and is powered by a dual supply at $\pm 15V$. The inverting input was connected to a DC signal varying from +5V to -5V while the non-inverting input was connected to ground.

---

[1]   Mouser 584-AD823ANZ
[2]   Mouser 584-AMP03GPZ

The second amplifier stage uses a power amplifier. This amplifier was connected in an inverting configuration. Originally, a PA341CE[3] was used and provided a gain of 10 using 5.6kΩ and 56kΩ resistors. It was connected to a dual power supply with $V_- = -12V$ and $V_+ = 110V$. A voltage this high proved unnecessary and a different chip was purchased. The replacement, an OPA548T[4], was powered by a single supply ranging from 0V to 60V. This chip (U2) was set up in an inverting configuration with a gain of 4.6, using 12kΩ (R3) and 56kΩ (R4) resistors. The inverting input was connected to the output of AMP03 (U1) through a 12kΩ resistor (R3). The non-inverting input was connected a constant voltage source. A capacitor (C9) was connected in parallel with the 56kΩ resistor to smooth any fluctuations of the output signal. The output current of the OPA548T can be controlled using the current-limiting pin. A 2.7MΩ (R6) resistor connected between the current-limiting pin and ground limits the output current to 21 mA. This eliminates the risk of damaging the crystal or the PID system. External influences can produce fluctuations in the shape of the crystal. A diode[5] (D2) was placed in series with the output of the OPA548T to prevent possible damage caused by these fluctuations.

A voltage reference for the power amplifier was needed to adjusted the output signal to the crystal. The original design used a 10kΩ potentiometer with $10\mu F$, $1\mu F$, and $0.1\mu F$ capacitors placed across the wiper and ground. The potentiometer and capacitors were replaced by an AMP03 (U3) in Its inverting input was connected to -15V through a 5.6kΩ resistor (R1). The non-inverting input was connected to ground. It was powered by a dual supply with ±15V. This configuration provided a low-impedance voltage source at a constant 5.46V for the power amplifier. The output was connected to the non-inverting stage of the power amplifier through a diode (D1). The final design can be seen in figure 4.1.

4.2 Testing

This system can supply a voltage ranging from 12V to 60V to the crystal. The first amplifier uses a voltage input from LabVIEW® that ranges between $V_{in} = \pm 5V$. The power amplifier uses a single supply setup ranging from 0V to 60V. The output voltage is governed by the equation

$$V_{out} = V_{adj} - (V_{in} - V_{adj})\frac{R_4}{R_3} \tag{4.1}$$

where V_{out} is the voltage output of each OPA548T, V_{adj} is 5.46V, and V_{in} is the voltage output of the each AMP03. A breadboard was used for prototyping each

---

[3] Digikey 598-1918-ND
[4] Mouser 595-OPA548T
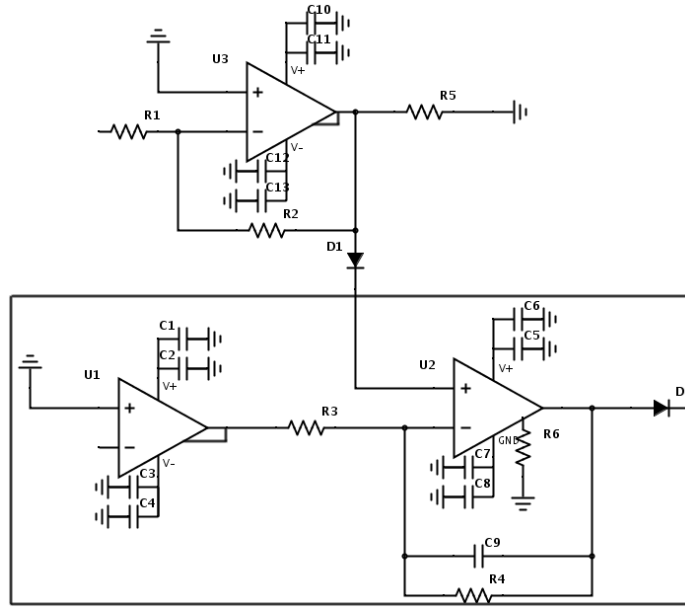[5] Digikey 497-2447-1-ND

Figure 4.1: Fluctuations in the power supply voltages were reduced using capacitors connected between ground and the supply pins of each amplifier. Three identical circuits were constructed using components within the boxed region. The output of each was dedicated to a single crystal.

design and test components. The voltage at each amplifier was measured and recorded while the input was varied. After the circuits were soldered to a PCB it was discovered that the power amplifiers' output did not vary. A drop in current supplied by the 60V supply was noticed when V_{adj} was measured. A 2.7MΩ resistor (R5) was connected to ground to replicate the voltmeters high-impedance connection to ground. Inputs and outputs of each circuit were soldered to BNC connectors. Supply voltages were connected to a 4-pin Hirose connector. Table 4.1 summarizes the results of the final assembly. Different input voltages were supplied to each input to test for interference between the three circuits. Output voltages measured agreed with the calculated values, indicating there is minimal interference between the circuits.

V_{in}	V_{calc}	V_1	V_2	V_3
-4	49.6	49.7	49.9	49.8
-2	40.2	40.4	40.6	40.4
0	30.9	31.2	31.3	31.2
2	21.6	21.7	21.8	21.7
4	12.2	12.4	12.4	12.4

Table 4.1: A calculated value V_{calc} is shown for each input voltage using equation 4.1 with V_{adj} =5.46V, R3=12kΩ, and R4=56kΩ. Each circuit was tested individually at various input voltages to ensure proper function.

Chapter 5

Conclusions and Future Directions

Ground state potential energy surfaces were plotted with previously [8, 9] calculated ground state potential energy surfaces of CaH^+. There was good agreement between the results of this work with previous data. The method used had the greatest effect on the shape of the potential energy surface. Calculations at higher levels of theory, such as CCSDT and CCSDTQ, may generate more accurate potential energy surfaces. Additionally, potential energy surfaces of excited states of the CaH^+ molecular ion can also be calculated using equation-of-motion coupled cluster methods (EOMCC).

Components for a UHV compatible oven were designed, fabricated, and assembled to vaporize solid calcium. Tests were conducted that resulted in the deposition of calcium vapor onto a glass slide. The path length and beam dispersion angle yield a calculated debris field radius of $r = 0.05"$. The measured debris field radius was $r = 0.15"$. The calculated debris field radius for the current oven setup is $r = 0.06"$, which could lead to deposition onto the trap electrodes. Longer supporting rods could be fabricated to increase the distance between the oven opening and the skimmer. This would decrease the beam dispersion angle, reducing the debris field radius.

Three stable high voltage sources were designed and constructed to drive three PZT crystals. This system enables three crystals to be driven from a single high voltage supply. Each output ranged from 12V to 60V using an input signal $V_{in} = \pm 5V$. The circuit will be used to precisely control the diffraction grating angle for each laser using a voltage signal from computer-controlled software.

Appendix

This appendix summarizes the content and syntax of files that were used to generate the potential energy surfaces contained in chapter 2. Detailed explanations of the content within the input and outputs files for Gaussian 09 and NWChem can be found within their respective user manuals. Descriptions and usage of the UNIX commands used for the shell scripts found in this appendix can be found using their respective `man` commands.

Sample Gaussian input

The following lines of text are interpreted as input by the *ab initio* quantum chemistry simulation software suite Gaussian 09. The first line indicates the desired method and basis set to be used. Additional options can be added to this line to indicate specific tasks to be performed during the calculation.

```
#CCSD(T,Full)/cc-PV5Z

CaH

1 1
Ca
H 1 0.5
```

This specific calculation is for a CCSD calculation that includes options to account for perturbative triples and core electron orbitals. The basis set to be used is specified after the method. The next line is the "name" of the calculation, following by a line with two numbers. These numbers indicated the spin multiplicity and charge of the system, respectively. The following two lines make what is known as a z-matrix. This matrix is an abstract representation of the the geometry of the system. The z-matrix above indicates a calcium atom centered at the origin that is bonded to a hydrogen atom located at $z = 0.5$Å.

Sample NwChem input

The following lines of text are interpreted as input by another *ab initio* quantum chemistry software suite NWChem. The geometry of the system, specified in lines 3 through 7, is defined by the position of its constituent atoms in a rectangular coordinate space. Basis sets for each atom are specified in lines 8 through 11. The calculations performed are divided into tasks and carried out by related modules within NWChem. Each task may contain specific options that are interpreted by the modules.

```
start tce_cc
memory stack 100 mb heap 100 mb global 5000 mb verify
geometry
 symmetry c2v
  Ca  0.0  0.0  -0.25
  H   0.0  0.0   0.25
end
basis spherical
  Ca  library cc-pcvqz
  H   library cc-pvqz
end
charge 1
scf
  rohf
  singlet
  thresh 1.0e-10
  tol2e 1.0e-10
  maxiter 100
end
tce
  ccsd(t)
  thresh 1.0e-7
  io ga
  tilesize 18
  lshift 0.3
 end
task tce energy
```

This specific input file performs two sequential calculations for the CaH^+ molecular ion. Each constituent atom of the system lies on the z-axis and are separated by 0.5Å. First, an SCF calculation is performed. The energy obtained from this calculation is then used by the second task. The final line commands NWChem to perform a CCSD(T) calculation to obtain the energy of this particular geometry using the

tensor contraction module (TCE). For more information about each task and their associated options, see the NWChem website.

Sample shell scripts

Shell scripts were employed for several purposes to facilitate the generation of multiple input files, submit jobs on the Palmetto Cluster, and to extract data from the resulting output files.

```
#!/bin/zsh
x=1
y=0.5
while (( x < 201 )) {
  echo -e "#CCSD(T,Full)/cc-PVDZ \n\nCaH\n\n1 1\nCa\nH 1 $y\n" > $x.com;
  let x=x+1;
  let y=y+0.05;
}
```

The above zsh script generates sequentially numbered input files for Gaussian 09. Each .com file, numbered 1 through 200, corresponds to a particular geometry. These input files can then be submitted to the Cluster individually, for calculations at a single geometry, or in an array.

```
#!/bin/bash

#PBS -N ex-g09
#PBS -l select=1:ncpus=8:mpiprocs=8:mem=8gb:interconnect=mx,walltime=00:59:59
#PBS -j oe
#PBS -J 1-200:1

module add gaussian/g09

cd $PBS_O_WORKDIR
cp ${PBS_ARRAY_INDEX}.com $TMPDIR
cd $TMPDIR

g09 < ${PBS_ARRAY_INDEX}.com > ${PBS_ARRAY_INDEX}.out

cp ${PBS_ARRAY_INDEX}.out $PBS_O_WORKDIR
```

The above pbs file is a bash script that submits an array of 200 jobs to the Cluster. Line 3 contains the options that are used for each job. This particular job array is used perform a calculation using Gaussian 09. The input files are copied from the working

directory, where the pbs file is located, into a temporary directory on a particular node. Once the calculation has completed, the output file is copied to the working directory. If the calculation fails or exceeds the time limit specified in line 3, the job is aborted. An output or log file is copied to the working directory to provide the user with some insight about the potential error. For a detailed overview of the Cluster and its capabilities, see the associated website.

```bash
#!/bin/bash
x=1
while [ $x -lt 201 ]; do
  distance=$(grep 'H  1' $x.out -C 0 -A 1 | tail -n 2 | awk '{print $3}') &&
  val1=$(grep ' SCF Done:  E(RHF) =' $x.out -C 1 -B 0 | awk '{print $5}') &&
  echo $distance $val1
  let x=x+1
done
```

Output files generated by both Gaussian 09 and NWChem contain a large amount of text. Sifting through each file individually to extract the relevant data is not feasible. The above bash script uses three common UNIX commands to extract the relevant data: grep, tail, and awk. If the specified string is found for each of the defined variables, each is printed to the user terminal with the echo command. If the string is absent from the file, the echo command prints a blank in place of the desired text. The above script extracts the system geometry and SCF energy from Gaussian 09 output files numbered from 1 to 200.

Bibliography

[1] T. Rosenband, D. B. Hume, P. O. Schmidt, C. W. Chou, A. Brusch, L. Lorini, W. H. Oskay, R. E. Drullinger, T. M. Fortier, J. E. Stalnaker, S. A. Diddams, W. C. Swann, N. R. Newbury, W. M. Itano, D. J. Wineland, and J. C. Bergquist. Frequency ratio of al+ and hg+ single-ion optical clocks; metrology at the 17th decimal place. *Science*, 319(5871):1808–1812, 2008.

[2] Masatoshi Kajita and Yoshiki Moriwaki. Proposed detection of variation in m p / m e using a vibrational transition frequency of a cah + ion. *Journal of Physics B: Atomic, Molecular and Optical Physics*, 42(15):154022, 2009.

[3] Wayne M Itano, J C Bergquist, J J Bollinger, and D J Wineland. Cooling methods in ion traps. *Physica Scripta*, 1995(T59):106, 1995.

[4] A. Boutalib and F. X. Gadea. Ab initio adiabatic and diabatic potential energy curves of the lih molecule. *The Journal of Chemical Physics*, 97(2):1144–1156, 1992.

[5] P. Fuentealba, O. Reyes, H. Stoll, and H. Preuss. Ground state properties of alkali and alkaline earth hydrides. *The Journal of Chemical Physics*, 87(9):5338–5345, 1987.

[6] Wolfgang Muller, Joachim Flesch, and Wilfried Meyer. Treatment of intershell correlation effects in ab initio calculations by use of core polarization potentials. method and application to alkali and alkaline earth atoms. *The Journal of Chemical Physics*, 80(7):3297–3310, 1984.

[7] Mireille Aymar and Olivier Dulieu. The electronic structure of the alkaline-earth-atom (ca, sr, ba) hydride molecular ions. *Journal of Physics B: Atomic, Molecular and Optical Physics*, 45(21):215103, 2012.

[8] Minori Abe, Yoshiki Moriwaki, Masahiko Hada, and Masatoshi Kajita. Ab initio study on potential energy curves of electronic ground and excited states of 40cah+ molecule. *Chemical Physics Letters*, 521(0):31 – 35, 2012.

[9] H. Habli, H. Ghalla, B. Oujia, and F.X. Gadéa. Ab initio study of spectroscopic properties of the calcium hydride molecular ion. *The European Physical Journal D*, 64(1):5–19, 2011.

[10] M. J. Frisch, G. W. Trucks, H. B. Schlegel, G. E. Scuseria, M. A. Robb, J. R. Cheeseman, G. Scalmani, V. Barone, B. Mennucci, G. A. Petersson, H. Nakatsuji, M. Caricato, X. Li, H. P. Hratchian, A. F. Izmaylov, J. Bloino, G. Zheng, J. L. Sonnenberg, M. Hada, M. Ehara, K. Toyota, R. Fukuda, J. Hasegawa, M. Ishida, T. Nakajima, Y. Honda, O. Kitao, H. Nakai, T. Vreven, J. A. Montgomery, Jr., J. E. Peralta, F. Ogliaro, M. Bearpark, J. J. Heyd, E. Brothers, K. N. Kudin, V. N. Staroverov, R. Kobayashi, J. Normand, K. Raghavachari, A. Rendell, J. C. Burant, S. S. Iyengar, J. Tomasi, M. Cossi, N. Rega, J. M. Millam, M. Klene, J. E. Knox, J. B. Cross, V. Bakken, C. Adamo, J. Jaramillo, R. Gomperts, R. E. Stratmann, O. Yazyev, A. J. Austin, R. Cammi, C. Pomelli, J. W. Ochterski, R. L. Martin, K. Morokuma, V. G. Zakrzewski, G. A. Voth, P. Salvador, J. J. Dannenberg, S. Dapprich, A. D. Daniels, Ö. Farkas, J. B. Foresman, J. V. Ortiz, J. Cioslowski, and D. J. Fox. Gaussian 09 Revision D.01. Gaussian Inc. Wallingford CT 2009.

[11] N. Govind K. Kowalski T.P. Straatsma H.J.J. van Dam D. Wang J. Nieplocha E. Apra T.L. Windus W.A. de Jong M. Valiev, E.J. Bylaska. NWChem: a comprehensive and scalable open-source solution for large scale molecular simulations. *Comput. Phys. Commun.*, 181(1477), 2010. doi:10.1016/j.cpc.2010.04.018.

[12] I.N. Levine. *Quantum Mechanics and Molecular Electronic Structure*. Allyn and Bacon chemistry series. Allyn and Bacon, 1970.

[13] A. Szabo and N.S. Ostlund. *Modern Quantum Chemistry: Introduction to Advanced Electronic Structure Theory*. Dover Books on Chemistry Series. Dover Publications, 1996.

[14] G.W. Richards. *Ab initio Molecular Orbital Calculations for Chemists*. Clarendon Press (Oxford University Press), 1983.

[15] F. Jensen. *Introduction to Computational Chemistry*. Wiley, 2013.

[16] M. Ziolkowski. *Local Correlation Approach for Coupled-Cluster Methods*. PhD thesis, Aarhus University, 2009.

[17] Jacek Koput and Kirk A. Peterson. Ab initio potential energy surface and vibrational-rotational energy levels of caoh. *The Journal of Physical Chemistry A*, 106(41):9595–9599, 2002.

[18] Thom H. Dunning. Gaussian basis sets for use in correlated molecular calculations. i. the atoms boron through neon and hydrogen. *The Journal of Chemical Physics*, 90(2):1007–1023, 1989.

[19] Donald G. Truhlar. Basis set extrapolation. *Chemical Physics Letters*, 294(1-3):45–48, 1998.

[20] Asger Halkier, Trygve Helgaker, Poul Jorgensen, Wim Klopper, Henrik Koch, Jeppe Olsen, and Angela K. Wilson. Basis set convergence in correlated

calculations on ne, n2, and h2o. *Chemical Physics Letters*, 286(3-4):243–252, 1998.

[21] P. Herskind. *Cavity Quantum Electrodynamics with Ion Coulomb Crystals*. PhD thesis, Aarhus University, 2008.

[22] M. Hermansen. Low-noise piezoelectric driver for external cavity diode lasers, April 2012.